

# Multi-Peaked Non-Thermal Light Curves from Magnetar-Powered Gamma-Ray Bursts

Conor M. B. Omand  <sup>1</sup>★ Nikhil Sarin  <sup>2,3</sup> and Gavin P. Lamb  <sup>1</sup>

<sup>1</sup>*Astrophysics Research Institute, Liverpool John Moores University, Liverpool Science Park IC2, 146 Brownlow Hill, Liverpool, UK, L3 5R*

<sup>2</sup>*The Oskar Klein Centre, Department of Physics, Stockholm University, AlbaNova, SE-106 91 Stockholm, Sweden*

<sup>3</sup>*Nordita, Stockholm University and KTH Royal Institute of Technology Hannes Alfvéns väg 12, SE-106 91 Stockholm, Sweden*

arXiv:2412.12272v1 [astro-ph.HE] 16 Dec 2024

Accepted XXX. Received YYY; in original form ZZZ

## ABSTRACT

Binary neutron star mergers and collapsing massive stars can both create millisecond magnetars. Such magnetars are candidate engines to power gamma-ray bursts (GRBs). The non-thermal light curve of the resulting transients can exhibit multiple components, including: the GRB afterglow, pulsar wind nebula (PWN), and ejecta afterglow. We derive the timescales for the peak of each component and show that the PWN is detectable at radio frequencies, dominating the emission for  $\sim 6$  years for supernova/long GRBs (SN/LGRBs) and  $\sim 100$  days for kilonova/short GRBs (KN/SGRBs) at 1 GHz, and  $\sim 1$  year for SN/LGRBs and  $\sim 15$  days for KN/SGRBs at 100 GHz. The PWN emission has an exponential, frequency-dependent rise to peak that cannot be replicated by an ejecta afterglow. We show that PWNe in SN/LGRBs can be detected out to  $z \sim 0.06$  with current instruments and  $z \sim 0.3$  with next-generation instruments and PWNe in KN/SGRBs can be detected out to  $z \sim 0.3$  with current instruments and  $z \sim 1.5$  with next-generation instruments. We find that the optimal strategy for detecting PWNe in these systems is a multi-band, high cadence radio follow-up of nearby KN/SGRBs with an x-ray plateau or extended prompt emission from 10 – 100 days post-burst.

**Key words:** stars: magnetars, transients: gamma-ray bursts, transients: neutron star mergers, transients: supernovae, radiation mechanisms: non-thermal

## 1 INTRODUCTION

Gamma-ray bursts (GRBs) are short flashes of high-energy radiation formed within relativistic jets (Piran 2004; Gehrels & Mészáros 2012; Zhang 2018). They are typically divided into two categories based on the duration of their prompt emission, with short GRBs (SGRBs) having a duration of  $T_{90} \lesssim 2$  s and long GRBs (LGRBs) having a duration of  $T_{90} \gtrsim 2$  s (Kouveliotou et al. 1993), where  $T_{90}$  is the timescale over which 90% of the background-subtracted counts are observed. The two GRB classes also show differences in their spectra, with SGRBs typically showing harder spectra than LGRBs (Kouveliotou et al. 1993). This dichotomy supports the idea that these distinct GRB classes arise from different progenitor channels, with SGRBs originating from compact object mergers (Lattimer & Schramm 1976; Blinnikov et al. 1984; Eichler et al. 1989) and LGRBs originating from the collapse of massive stars (MacFadyen & Woosley 1999; MacFadyen et al. 2001). There is observational evidence that supports this distinction; LGRBs have been associated with supernovae (SNe) (e.g., Gendre et al. 2013; Nakauchi et al. 2013; Levan et al. 2014; Cano et al. 2017), and several SGRBs associated with kilonovae (KNe) (e.g., Tanvir et al. 2013; Yang et al. 2015; Jin et al. 2016, 2020; Lamb et al. 2019b; Fong et al. 2021; Zhou et al. 2023; Zhu et al. 2023), including the SGRB GRB170817A accompanying the binary neutron star (BNS) merger that produced

GW170817 (Abbott et al. 2017a). However, two recent LGRBs have been inferred to have originated from BNS mergers due to emission resembling that of a kilonova (Rastinejad et al. 2022; Levan et al. 2024), casting some doubt on the robustness of this classification scheme.

Most models for launching relativistic jets that produce GRBs require angular momentum and energy from a compact object – accretion disk system. The compact object can either be a black hole or a highly magnetized neutron star, known as a magnetar (Duncan & Thompson 1992). For black holes, the energy can be extracted from the black hole spin (Blandford & Znajek 1977) or accretion disk (Blandford & Payne 1982) via a twisted magnetic field, or neutrino winds from the accretion disk (e.g. Popham et al. 1999). While magnetars can launch jets via similar processes, they can also launch jets from a magnetorotational mechanism with strong dipolar or toroidal fields (Mösta et al. 2020; Bugli et al. 2021), or from strong propeller-driven outflows (Illarionov & Sunyaev 1975; Lovelace et al. 1999; Romanova et al. 2005).

When the relativistic jet sweeps up material and starts to decelerate, a broadband synchrotron and inverse Compton GRB afterglow is emitted (Paczynski & Rhoads 1993; Sari et al. 1998; Piran 2004; Zhang & Mészáros 2004; Zhang et al. 2006; MAGIC Collaboration et al. 2019). The temporal lightcurve of this afterglow will be dominated by the jet core for on-axis observers and will depend on the wider structure of the jet for off-axis observers (Granot et al. 2002; Rossi et al. 2002). While the afterglow emission is mostly

★ E-mail: c.m.omand@ljmu.ac.uk

predicted to rise and fall with power laws (Sari et al. 1998), several other phenomena have been detected in the afterglow emission. One of these phenomena are X-ray plateaus, where the flux of the X-ray afterglow transitions from an initial steep decay, to a very shallow decay or plateau, back to a steep decay (Nousek et al. 2006; O'Brien et al. 2006; Rowlinson et al. 2013; Dainotti et al. 2017). This has been suggested to be due to energy injection from a central magnetar (Troja et al. 2007; Rowlinson et al. 2013; Gompertz et al. 2014; Stratta et al. 2018; Sarin et al. 2019). Another GRB phenomenon potentially linked to a magnetar central engine is extended emission (Metzger et al. 2008; Bucciantini et al. 2012; Gompertz et al. 2013, 2014; Gibson et al. 2017), where the prompt GRB emission is followed by a lower luminosity signal that can be several times longer than the prompt emission and extends to softer energies (Norris & Bonnell 2006; Bostancı et al. 2013; Kaneko et al. 2015).

The wind from the spin-down of a rotating neutron star will also produce a pulsar wind nebula (PWN) on the interior of the ejecta that is a broadband synchrotron and inverse Compton emitter. The thermalization of PWN emission in the ejecta is thought to power a number of transients, including superluminous supernovae (SLSNe) (Nicholl et al. 2017; Kangas et al. 2022; West et al. 2023; Gomez et al. 2024; Gkini et al. 2024) and some broad-line SN-Ic (SNe Ic-BL) (Mazzali et al. 2014; Greiner et al. 2015; Wang et al. 2017; Omand & Sarin 2024). The PWN can also be detected in radio (Murase et al. 2015; Omand et al. 2018; Eftekhari et al. 2019; Law et al. 2019; Mondal et al. 2020; Eftekhari et al. 2021), can cause an infrared excess by heating up dust in the ejecta (Omand et al. 2019; Chen et al. 2021; Sun et al. 2022), spectral differences by ionizing the ejecta (Chevalier & Fransson 1992; Jerkstrand et al. 2017; Omand & Jerkstrand 2023; Dessart 2024), and polarization signals by expanding the ejecta asymmetrically (Inserra et al. 2016; Saito et al. 2020; Poidevin et al. 2022; Pursiainen et al. 2022; Poidevin et al. 2023; Pursiainen et al. 2023). The PWN can also cause instabilities in the ejecta (Chen et al. 2016; Suzuki & Maeda 2017, 2021) that results in a filamentary ejecta structure similar to the Crab Nebula (Clark et al. 1983; Bietenholz et al. 1991; Temim et al. 2006; Omand et al. 2024).

The ejecta from a transient accompanying a GRB, a supernova or a kilonova, can produce its own afterglow once it sweeps up enough mass. X-ray observations of GRB170817A have shown tentative evidence for a re-brightening of the afterglow at late times potentially consistent with this scenario (Hajela et al. 2022; Troja et al. 2022). A few supernovae have been detected in radio at late times (e.g. van Dyk et al. 1994; Gaensler et al. 1997; Corsi et al. 2022; Kool et al. 2023; Margutti et al. 2023) and X-ray (e.g. Chevalier & Fransson 1994; Dwarkadas 2014; Bochenek et al. 2018), and some at much earlier times when dense circumstellar material (CSM) surrounds the progenitor (e.g. Smith et al. 2008; Fransson et al. 2014; Drout et al. 2016).

Magnetar-driven GRB systems should produce non-thermal emission from a GRB afterglow, PWN, and SN/KN afterglow (we refer to this as an ejecta afterglow), as well as thermal emission from the magnetar-heated ejecta. The timescale for these three non-thermal mechanisms can be significantly different, leading to the potential of detecting all three components separately. The GRB and ejecta afterglow both arise when the jet and ejecta sweep up an amount of mass comparable to themselves, but the jet is much faster and less massive, leading to the GRB afterglow peaking much earlier. The peak of the PWN emission is set by the opacity of the ejecta, which can vary greatly across bands due to the different absorption processes involved at different energies. However, for most energies, the PWN will peak sometime in between the GRB afterglow and ejecta afterglow, leading to a distinct third component. Previous ob-

servations searching for multiple components have only led to upper limits (e.g. Schroeder et al. 2020).

Here, we examine the emission for each component and show the multi-peaked non-thermal light curves that can result from such systems. In Section 2, we derive the scaling relations and fiducial timescales for the three components. In Section 3, we show the resulting light curves in radio and X-ray, and show that the magnetar signal can not be reproduced by an ejecta afterglow. In Section 4, we discuss strategies for observation, caveats and uncertainties of our approach, and analyze a few notable GRBs. Finally, in Section 5, we summarize our findings.

## 2 ANALYTIC TIMESCALE ESTIMATES

Here, we estimate the timescales of the peaks of each non-thermal component using simple analytic scalings at radio and X-ray frequencies. The fiducial timescales for each component in both the kilonova and supernova scenarios are summarized in Table 1.

### 2.1 GRB Afterglow

We estimate the peak timescale for an on-axis afterglow using the standard closure relations (Sari et al. 1998). We assume a fully adiabatic shock and that the afterglow is in the slow-cooling regime. The timescales where the cooling frequency  $\nu_c$  and the frequency at the minimum electron acceleration  $\nu_m$  cross the observed frequency  $\nu$  are

$$t_c \approx 7.3 \left( \frac{\epsilon_B}{0.01} \right)^{-3} \left( \frac{E_{\text{jet}}}{10^{52} \text{ erg}} \right)^{-1} \left( \frac{n_{\text{CSM}}}{1 \text{ cm}^{-3}} \right)^{-2} \left( \frac{\nu}{10^6 \text{ GHz}} \right)^{-2} \text{ days}, \quad (1)$$

$$t_m \approx 10 \left( \frac{\epsilon_B}{0.01} \right)^{1/3} \left( \frac{\epsilon_e}{0.1} \right)^{4/3} \left( \frac{E_{\text{jet}}}{10^{52} \text{ erg}} \right)^{1/3} \left( \frac{\nu}{10^6 \text{ GHz}} \right)^{-2/3} \text{ minutes}, \quad (2)$$

where  $\epsilon_B$  and  $\epsilon_e$  are the fractions of shock energy that go into magnetic field and leptons, respectively,  $E_{\text{jet}}$  is the energy of the jet, and  $n_{\text{CSM}}$  is the number density of the ambient medium. Whether the peak of the light curve is set by  $t_c$  or  $t_m$  is determined by which timescale is shorter, which can be determined by the critical frequency

$$\nu_{\text{crit}} \approx 1.8 \times 10^8 \left( \frac{\epsilon_B}{0.01} \right)^{-5/2} \left( \frac{\epsilon_e}{0.1} \right)^{-1} \left( \frac{E_{\text{jet}}}{10^{52} \text{ erg}} \right)^{-1} \left( \frac{n_{\text{CSM}}}{1 \text{ cm}^{-3}} \right)^{-3/2} \text{ GHz}. \quad (3)$$

For  $\nu > \nu_{\text{crit}}$  (the high-frequency light curve), the peak occurs at  $t_c$ , while for  $\nu < \nu_{\text{crit}}$  (the low-frequency light curve), the peak occurs at  $t_m$ . If these timescales are shorter than the jet deceleration timescale (Blandford & McKee 1976, 1977; Mészáros 2006)

$$t_{\text{dec,jet}} = 100 \left( \frac{E_{\text{jet}}}{10^{52} \text{ erg}} \right)^{1/3} \left( \frac{n_{\text{CSM}}}{1 \text{ cm}^{-3}} \right)^{-1/3} \left( \frac{\gamma_0}{100} \right)^{-8/3} \text{ s}, \quad (4)$$

where  $\gamma_0$  is the initial Lorentz factor of the jet, then the light curve will peak at the deceleration time. For a typical observed LGRB jet with  $\epsilon_e \sim 0.1$ ,  $\epsilon_B \sim 0.01$ ,  $E_{\text{jet}} \sim 10^{52}$  erg,  $\gamma_0 \sim 100$ , and  $n_{\text{CSM}} \sim 1 \text{ cm}^{-3}$  (Wang et al. 2015; Atteia et al. 2017), the critical frequency is  $\nu_{\text{crit}} \sim 2 \times 10^8 \text{ GHz} \approx 1 \text{ keV}$ , and the peak timescales in the radio bands are  $\sim 70$  days at 1 GHz and around 3 days at 100 GHz, while in the X-ray bands they are set by the deceleration time,  $\sim$

Transient	Component	1 GHz	100 GHz	1 keV	100 keV
SN/LGRB	GRB Afterglow	70 days	3 days	100 s	100 s
	PWN	10 yr	500 days	60 yr	100 days
	Ejecta Afterglow	80 yr	80 yr	80 yr	80 yr
KN/SGRB	GRB Afterglow	7 days	8 hours	20 s	20 s
	PWN	100 days	15 days	6 yr	2 days
	Ejecta Afterglow	3 yr	3 yr	3 yr	3 yr

**Table 1.** The peak timescale of each non-thermal component at various radio and X-ray bands for our fiducial parameters. The parameters used for estimating the timescales and the scaling relations for each value can be found in their respective sections.

100 s. For a typical observed SGRB, with the same  $\epsilon_e$ ,  $\epsilon_B$ ,  $\gamma_0$ , and  $n_{\text{CSM}}$ , but a lower jet energy of  $E_{\text{jet}} \sim 10^{50}$  erg (Fong et al. 2015), the critical frequency is  $\nu_{\text{crit}} \sim 2 \times 10^{11}$  GHz  $\sim 100$  keV, and the peak timescales in the radio bands are  $\sim 7$  days at 1 GHz and around 8 hours at 100 GHz, while in the X-ray bands they are set by the deceleration time,  $\sim 20$  s.

For an afterglow viewed from off-axis, the peak will be delayed compared to the same afterglow viewed on-axis. For  $\theta_{\text{obs}} \gg \theta_{\text{jet}}$ , the peak timescale will change  $\propto \theta_{\text{obs}}^{8/3}$ , regardless of the structure of the jet<sup>1</sup> (Nakar et al. 2002; Lamb & Kobayashi 2017; Xie et al. 2018; Ioka & Nakamura 2018).

## 2.2 PWN

We estimate the peak timescale for a PWN using the relations derived by the model in Appendix A. Due to the PWN emission being produced shortly after the explosion from the inside of the ejecta, the timescale for the observed peak is set by when the optical depth of the ejecta in a specific band drops to unity. For radio emission, the key process is free-free absorption, although synchrotron self-absorption can be key in certain regions of parameter space; for soft X-rays, it is photoelectric absorption; and for hard X-rays, it is Compton scattering.

Taking Equations A9, A12 and A13 for optical depth and solving for the timescales where  $\tau = 1$  gives

$$t_{\text{esc,ff}} \approx 130 \left( \frac{M_{\text{ej}}}{M_{\odot}} \right)^{2/5} \left( \frac{Y_{\text{fe}}}{0.05} \right)^{2/5} \left( \frac{\bar{Z}}{10} \right)^{2/5} \left( \frac{v_{\text{ej}}}{10^5 \text{ km s}^{-1}} \right)^{-1} \left( \frac{\nu}{10 \text{ GHz}} \right)^{-0.42} \text{ days}, \quad (5)$$

$$t_{\text{esc,pe}} \approx 80 \left( \frac{M_{\text{ej}}}{M_{\odot}} \right)^{1/2} \left( \frac{\bar{Z}}{10} \right) \left( \frac{v_{\text{ej}}}{10^5 \text{ km s}^{-1}} \right)^{-1} \left( \frac{h\nu}{10 \text{ keV}} \right)^{-3/2} \text{ days}, \quad (6)$$

$$t_{\text{esc,comp}} \approx 10 \left( \frac{M_{\text{ej}}}{M_{\odot}} \right)^{1/2} \left( \frac{Y_{\text{e}}}{0.5} \right)^{1/2} \left( \frac{v_{\text{ej}}}{10^5 \text{ km s}^{-1}} \right)^{-1} \left( \frac{\sigma_{\text{KN}}(\nu)}{\sigma_T} \right)^{1/2} \text{ days}, \quad (7)$$

where  $Y_{\text{fe}}$  is the free electron fraction (defined in Equation A11) within the ejecta,  $\bar{Z}$  is the average atomic number of the ejected material,  $v_{\text{ej}}$  is the ejecta velocity,  $Y_e$  is the electron fraction within the ejecta, and  $\sigma_{\text{KN}}$  and  $\sigma_T$  are the Klein-Nishina and Thompson cross-sections, respectively.

For a fiducial GRB-SN with parameters chosen to be broadly

<sup>1</sup> This applies as long as the jet has a core-dominated structure.

consistent with observations (Taddia et al. 2019; Srinivasaragavan et al. 2024), the ejecta mass and velocity will be around  $5 M_{\odot}$  and 20 000 km s $^{-1}$ , giving a total kinetic energy of  $\sim 10^{52}$  erg. The ejecta is assumed to consist of singly ionized oxygen, which has  $Y_{\text{e}} \sim 0.5$ ,  $\bar{Z} \sim 8$ , and  $Y_{\text{fe}} \sim 1/16$ . Given these parameters, the peak timescale is  $\sim 10$  years at 1 GHz,  $\sim 500$  days at 100 GHz,  $\sim 60$  years at 1 keV, and  $\sim 100$  days at 100 keV.

For our fiducial magnetar-driven kilonova, motivated by previous modeling efforts and numerical simulations (Yu et al. 2013; Siegel & Metzger 2017; Metzger 2019; Margalit & Metzger 2019; Sarin et al. 2022; Ai et al. 2024), the ejecta mass and velocity will be around  $0.1 M_{\odot}$  and  $0.5c$ , giving a total kinetic energy of  $\sim 2 \times 10^{52}$  erg. The ejecta is assumed to have  $Y_{\text{e}} \sim 0.4$ ,  $\bar{Z} \sim 40$ , and  $Y_{\text{fe}} \sim 0.02$ , which is broadly consistent with r-process nucleosynthesis calculations (Foucart et al. 2016; Roberts et al. 2017; Vlasov et al. 2017). Given these parameters, the peak timescale is  $\sim 100$  days at 1 GHz,  $\sim 15$  days at 100 GHz,  $\sim 6$  years at 1 keV, and  $\sim 2$  days at 100 keV.

## 2.3 Ejecta Afterglow

The emission from the ejecta-CSM interaction will peak around the time when the ejecta sweeps up a mass comparable to itself, known as the ejecta deceleration timescale. Following Nakar & Piran (2011) (see also Hotokezaka et al. 2016), a spherical outflow with energy  $E_{\text{ej}}$  and velocity  $c\beta_0$  propagating into a medium of density  $n_{\text{CSM}}$  will begin to decelerate at a radius of

$$R_{\text{dec}} \approx 10^{18} \left( \frac{E_{\text{ej}}}{10^{52} \text{ erg}} \right)^{1/3} \left( \frac{n_{\text{CSM}}}{1 \text{ cm}^{-3}} \right)^{-1/3} \beta_0^{-2/3} \text{ cm} \quad (8)$$

on a timescale of

$$t_{\text{dec,ejecta}} = \frac{R_{\text{dec}}}{c\beta_0} \approx 300 \left( \frac{E_{\text{ej}}}{10^{52} \text{ erg}} \right)^{1/3} \left( \frac{n_{\text{CSM}}}{1 \text{ cm}^{-3}} \right)^{-1/3} \beta_0^{-5/3} \text{ days}. \quad (9)$$

The peak timescale can be longer if the observed frequency is below either the self-absorption frequency  $\nu_{\text{ssa}}$  or the synchrotron frequency at the minimum Lorentz factor  $\nu_m$  at the deceleration timescale. These frequencies have values

$$\nu_{\text{ssa}} \approx 1 \left( \frac{E_{\text{ej}}}{10^{49} \text{ erg}} \right)^{\frac{2}{3(4+p)}} \left( \frac{n_{\text{CSM}}}{1 \text{ cm}^{-3}} \right)^{\frac{14+3p}{6(4+p)}} \left( \frac{\epsilon_B}{0.1} \right)^{\frac{2+p}{2(4+p)}} \left( \frac{\epsilon_e}{0.1} \right)^{\frac{2(p-1)}{4+p}} \beta_0^{\frac{15p-10}{3(4+p)}} \text{ GHz} \quad (10)$$

$$\nu_m \approx 1 \left( \frac{n_{\text{CSM}}}{1 \text{ cm}^{-3}} \right)^{1/2} \left( \frac{\epsilon_B}{0.1} \right)^{1/2} \left( \frac{\epsilon_e}{0.1} \right)^2 \beta_0^5 \text{ GHz} \quad (11)$$

at  $t_{\text{dec}}$ , where  $p \sim 2.5$  is the index of the accelerated electrons  $dN/dy \propto \gamma^{-p}$ . For a fiducial GRB supernova ( $E_{\text{ej}} \sim 10^{52}$  erg,  $\beta_0 \sim 0.06$ ,  $n_{\text{CSM}} \sim 1 \text{ cm}^{-3}$ ,  $\epsilon_B = \epsilon_e \sim 0.1$ ) and for ejecta from a magnetar-driven kilonova ( $E_{\text{ej}} \sim 10^{52}$  erg,  $\beta_0 \sim 0.5$ ,  $n_{\text{CSM}} \sim 1$

$\text{cm}^{-3}$ ,  $\epsilon_B = \epsilon_e \sim 0.1$ ) (Nakar & Piran 2011; Sarin et al. 2022),  $\nu_{\text{ssa}}$  and  $\nu_m$  are both below 1 GHz, and thus all bands will peak at the deceleration timescale, which is  $\sim 3$  years for the kilonova and  $\sim 80$  years for the supernova.

### 3 MODELING

#### 3.1 Fiducial Light Curves

Here, we show the fiducial non-thermal light curves of SNe/LGRBs and KN/SGRBs at 1 GHz, 100 GHz, 1 keV, and 100 keV. The models are generated with Redback (Sarin et al. 2024) using the `tophat_redbck` (Lamb et al. 2018), PWN (This work, Appendix A), and `kilonova_afterglow_redbck` (Margalit & Piran 2020; Sarin et al. 2022) models for the GRB afterglow, PWN, and ejecta afterglow, respectively. These models for a distance of 100 Mpc are shown in Figure 1.

The GRB afterglow model is calculated using a jet opening angle of  $\theta_{\text{jet}} = 0.1$  radians, the spectral index  $p = 2.5$ , initial Lorentz factor  $\gamma_0 = 100$ ,  $\epsilon_e = 0.1$ ,  $\epsilon_B = 0.01$ , and a jet energy of  $E_{\text{jet}} = 10^{52}$  erg for the LGRB and  $10^{50}$  erg for the SGRB. The models are calculated with two values of  $n_{\text{CSM}}$ :  $1 \text{ cm}^{-3}$  and  $10^{-3} \text{ cm}^{-3}$ , representing the high and low ends of typical observed GRBs. The models are also calculated with two viewing angles,  $0^\circ$  and  $32^\circ$ , which are referred to as on- and off-axis respectively. The off-axis angle was chosen as  $32^\circ$  because it is the peak of the inclination distribution for gravitational wave detected sources, and therefore the most likely viewing angle for GW counterparts (Schutz 2011; Lamb & Kobayashi 2017).

The PWN model is calculated using a magnetar braking index<sup>2</sup>  $n = 3$ ,  $\epsilon_B = 10^{-2}$ , and  $\gamma_b = 10^{-5}$ . The supernova scenario is calculated with  $L_0 = 10^{48} \text{ erg s}^{-1}$ ,  $t_{\text{SD}} = 10^4 \text{ s}$ ,  $M_{\text{ej}} = 5M_\odot$  while the kilonova scenario is calculated with  $L_0 = 10^{50} \text{ erg s}^{-1}$ ,  $t_{\text{SD}} = 10^2 \text{ s}$ ,  $M_{\text{ej}} = 0.05M_\odot$ . The kilonova is also calculated with a different ejecta composition, with  $Y_e \sim 0.4$ ,  $\bar{Z} \sim 40$ , and  $Y_{\text{fe}} \sim 0.02$ .

The parameters for the ejecta afterglow are mostly shared with the other models, since  $n_{\text{CSM}}$  is already set in the GRB afterglow model,  $M_{\text{ej}}$  is set by the PWN model, and  $E_{\text{ej}}$  is calculated in the PWN model, and set by  $L_0$ ,  $t_{\text{SD}}$ , and  $M_{\text{ej}}$ . The partition parameters are set as  $\epsilon_e = \epsilon_B = 0.1$ , and the spectral index is taken as  $p = 2.5$ .

In radio bands, the PWN is always detectable for the fiducial magnetar-driven supernova. The viewing angle of the GRB does not impact the timescale of the detectability of the PWN due to the large difference in peak timescales. The PWN peak timescales of the model are  $\sim$  a few hundred days at 100 GHz and  $\sim$  a decade at 1 GHz, in agreement with what we derived in Section 2. The detectability window of the PWN depends on the ambient density, since both afterglow components decrease in luminosity in more rarefied environments, especially the ejecta afterglow. The GRB afterglow is always the dominant component at early times, and ejecta afterglow at late times. The PWN is the dominant component after  $\sim 6$  years at 1 GHz and after  $\sim 1$  year at 100 GHz, and it is the dominant component in both bands until  $\sim 30$  years in the high density medium and until  $> 300$  years in the low density medium.

The radio emission from the PWN in the fiducial magnetar-driven kilonova will be detectable in most situations, although in dense environments, the ejecta afterglow will have comparable luminosity at 1 GHz to the PWN at the PWN peak timescale. The GRB afterglow

is the dominant component at early times if the GRB is on-axis or in a dense ambient medium, but will be subdominant to the PWN in a diffuse medium for an off-axis observer. The peak timescale is set by synchrotron self-absorption at 1 GHz and free-free absorption at 100 GHz. The detectability window at 1 GHz in a high-density medium is  $\sim 40 - 150$  days, and for a low-density medium the window is  $\sim 30 - 1500$  days, while at 100 GHz the window for a high-density medium is 5 – 90 days and for a low density medium is 5 – 1500 days.

In X-rays, there are some regions of the parameter space where the PWN does not dominate the light curve on any timescale in a magnetar-driven supernova, due to the similar peak timescale to the ejecta afterglow. This is the case at 1 keV in a dense medium, and even in a low-density medium, the PWN will not be the dominant component until several decades post-explosion. At 100 keV, the PWN will be the dominant component from  $\sim 50$  days until  $> 30$  years, and will be preceded by the GRB in each case except for an off-axis afterglow in a high-density medium, which rises on the same timescale as the PWN but at a lower luminosity.

At 1 keV, the PWN in the fiducial magnetar-driven kilonova will never dominate over the kilonova afterglow. At 100 keV it dominates from  $< 1$  day until  $\sim 150$  days in a high-density medium and  $\sim 800$  days in a low-density medium.

#### 3.2 Inference on a Simulated Light Curve

To determine whether a pulsar wind nebula can be distinguished from an afterglow in data, we simulate and fit an observed radio light curve generated for the fiducial kilonova/SGRB using the REDBACK simulation workflow at 1 and 100 GHz for up to 100 days post explosion. The light curves are observed ten times over the timespan at each frequency. The distance to the transient is 100 Mpc, giving a redshift of  $z = 0.024$ ; the neutron star merger that causes this transient would thus also be detectable with current gravitational wave detectors (Abbott et al. 2020).

Inference is performed using REDBACK (Sarin et al. 2024) with the PYMULTINEST sampler (Buchner et al. 2014) implemented in BILBY (Ashton et al. 2019). We sample in flux density with a Gaussian likelihood. To gauge whether the pulsar wind nebula is needed to explain the observed emission, we implement a Slab-Spike prior (Malsiner-Walli & Wagner 2018) on the initial pulsar wind nebula luminosity  $L_0$ , which imposes a dirac-delta function onto an already existing prior. We give the spike 10% of the probability of the prior and place it at the lowest value of  $L_0$  within the prior. Having a large probability of a low value of  $L_0$  allows us to test if the emission can be reproduced with the PWN effectively turned off. A list of the parameters varied in the inference, as well as the median and  $1\sigma$  values of the posterior, is found in Table 2. Other parameter values are kept constant at their fiducial values (see Section 3.1).

The fitted data is shown in Figure 2 and the posterior is shown in Figure B1. The posteriors for the afterglow parameters  $E_{\text{jet}}$ ,  $\epsilon_{e,\text{GRB}}$ ,  $\epsilon_{B,\text{GRB}}$  and as well as  $n$ ,  $\epsilon_{B,\text{PWN}}$ , and  $\gamma_b$ , are all found to be within around  $1\sigma$  of the injected parameters.  $\theta_{\text{obs}}$  and  $n_{\text{CSM}}$  are more than  $1\sigma$  away, but are correlated, while  $\epsilon_{e,\text{ejecta}}$  and  $\epsilon_{B,\text{ejecta}}$  are not well constrained due to the signal lacking an ejecta afterglow component. The one-dimensional posteriors for  $L_0$  and  $t_{\text{SD}}$  underestimate and overestimate the injected values respectively, although the degeneracy between them is clear in the two-dimensional posterior. The ejecta mass is also significantly underestimated. These three parameters all show strong correlation and have wide priors with the injected value close to the edge of the prior. The escape time (Equation 5) shows a dependence on both ejecta mass and velocity, so the lower

<sup>2</sup> The braking index  $n$  parameterizes the time dependence of the magnetar spin-down (see Equation A1). The value  $n = 3$  corresponds to vacuum dipole spin down.

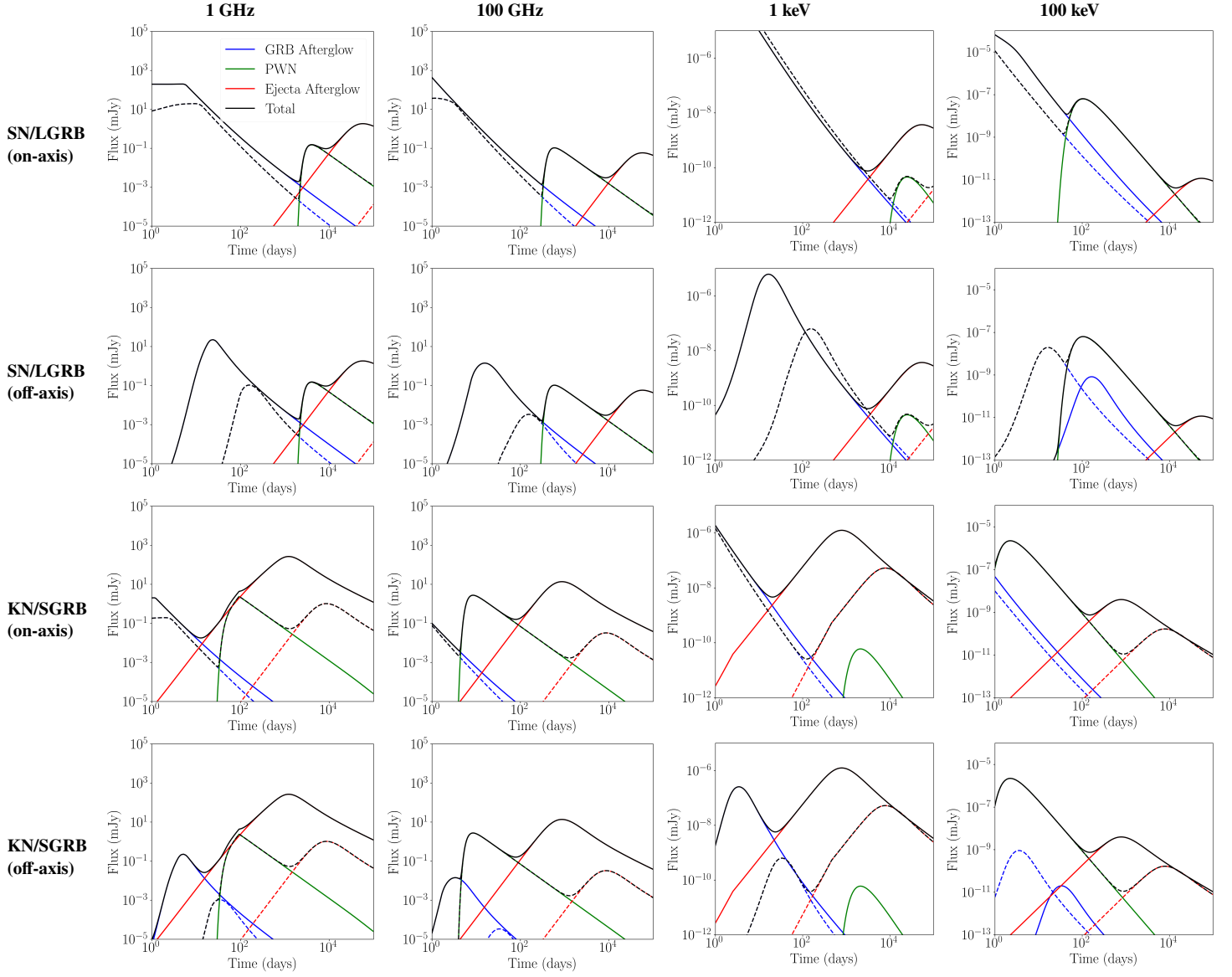


**Figure 1.** Non-thermal light curves for our fiducial magnetar-driven supernovae and kilonovae, with on- and off-axis GRBs, in radio and X-ray. Each panel shows the GRB afterglow (blue), PWN (green), ejecta afterglow (red), and total emission (black). The solid and dashed lines indicate the density of the ambient medium  $n_{\text{CSM}}$  to be 1 and  $10^{-3} \text{ cm}^{-3}$  respectively. The off-axis afterglow is taken from an observer angle of  $32^\circ$ . The transient is assumed to be at 100 Mpc ( $z = 0.024$ ).

Parameter	Definition	Units	Injected Value	Prior	1D Posterior Values
$\theta_v$	Viewing Angle	Radians	0.1	Sine[0, $\pi/2$ ]	$0.34^{+0.10}_{-0.14}$
$E_{\text{jet}}$	Jet Energy (Isotropic Equivalent)	erg	$10^{50}$	L[ $10^{46}, 10^{53}$ ]	$L(49.87^{+0.65}_{-0.45})$
$\epsilon_{e,\text{GRB}}$	Lepton Energy Parameter (GRB)		0.1	L[ $10^{-5}, 1$ ]	$L(-1.07^{+0.44}_{-1.30})$
$\epsilon_{B,\text{GRB}}$	Magnetization Parameter (GRB)		0.01	L[ $10^{-5}, 1$ ]	$L(-1.38^{+0.95}_{-1.68})$
$n_{\text{CSM}}$	CSM number density	$\text{cm}^{-3}$	$10^{-2}$	L[ $10^{-5}, 10^2$ ]	$L(0.74^{+0.75}_{-1.15})$
$L_0$	Initial Magnetar Spin-Down Luminosity	$\text{erg s}^{-1}$	$10^{50}$	S[ $10^{40}, L[10^{40}, 10^{51}]$ ]	$L(45.46^{+1.15}_{-1.01})$
$t_{\text{SD}}$	Spin-Down Time	s	$10^2$	L[ $10, 10^8$ ]	$L(4.35^{+0.69}_{-0.90})$
$M_{\text{ej}}$	Ejecta Mass	$M_\odot$	0.05	L[ $0.01, 100$ ]	$0.02^{+0.00}_{-0.00}$
$n$	Magnetar Braking Index		3	U[ $1.5, 10$ ]	$2.80^{+0.26}_{-0.25}$
$\epsilon_{B,\text{PWN}}$	Magnetization Parameter (PWN)		$10^{-2}$	L[ $10^{-7}, 1$ ]	$L(-1.29^{+0.60}_{-0.56})$
$\gamma_b$	Electron Injection Lorentz Factor		$10^5$	L[ $10^2, 10^8$ ]	$L(4.77^{+1.73}_{-1.55})$
$\epsilon_{e,\text{ejecta}}$	Lepton Energy Parameter (Ejecta)		0.1	L[ $10^{-5}, 1$ ]	$L(-3.41^{+1.47}_{-1.05})$
$\epsilon_{B,\text{ejecta}}$	Magnetization Parameter (Ejecta)		0.1	L[ $10^{-5}, 1$ ]	$L(-3.21^{+1.67}_{-1.18})$

**Table 2.** The parameters and priors used in this study. Priors are either uniform (U) log-uniform (L), sine (Sine), or Slab-Spike (S). The values shown for the posterior are the median and  $1\sigma$  uncertainties. Posterior values denoted with L are given in log-space. The full posterior is shown in Figure B1.

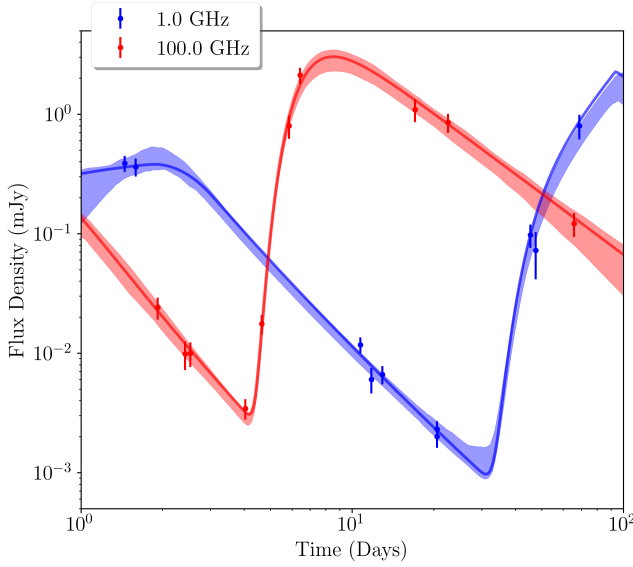


**Figure 2.** The fitted radio light curve for the simulated kilonova/SGRB for both 1 and 100 GHz. The solid line shows the model with the highest likelihood while the shaded region shows the 90% confidence interval.

inferred ejecta mass implies that the ejecta in the inferred model must have lower velocity than in the injected model, which is consistent with a lower  $L_0$  and higher  $t_{SD}$ . This example shows the sensitivity of the inferred parameters to the intrinsic noise of the measurement. Other estimates of  $M_{ej}$  or  $v_{ej}$  in a real system, either from gravitational wave data (Abbott et al. 2019), kilonova light curve modeling (Yu et al. 2013; Metzger 2019; Sarin et al. 2022), or kilonova spectroscopy (Hotokezaka et al. 2021; Pognan et al. 2023), would help get a more accurate estimate of the PWN and ejecta parameters.

The posterior for  $L_0$  shows no probability at  $10^{40}$  erg, showing that it is unlikely that this emission can be reproduced without a strong PWN. The main features that can not be reproduced by an ejecta afterglow are the frequency-dependent peak timescales and the fast rise from only GRB afterglow emission to PWN peak. The ejecta afterglow emission timescale can be frequency-dependent if either the self-absorption frequency or synchrotron frequency of the minimum Lorentz factor is higher than the observed frequency, which can happen at low frequencies in atypical cases. This would cause a dependence of either  $t_{peak} \propto v_{obs}^{-1/3}$  if  $v_m$  is higher or  $t_{peak} \propto v_{obs}^{-(4+p)/(3p-2)}$  if  $v_{ssa}$  is higher (Nakar & Piran 2011), which could mimic the  $t_{peak} \propto v_{obs}^{-0.42}$  expected for a PWN. However, the rising flux for an ejecta afterglow is a power law which becomes slower ( $F_\nu \propto t^{1.5}$  as opposed to  $F_\nu \propto t^3$ ) under the conditions where  $t_{peak}$  becomes frequency-dependent (Nakar & Piran 2011). The ejecta afterglow rising flux also contrasts with the PWN rising flux, which is an exponential rise due to being caused by optical depth effects. While this can be used to distinguish between the two scenarios, one needs multiple extremely high cadence observations during the light curve rise to distinguish them via the rise index alone.

## 4 DISCUSSION

Although the PWN can be the dominant emission component at certain times and frequencies, these PWNe are still not bright enough to be seen at large redshifts. The detection limit for NuSTAR in hard

x-rays is roughly 1 nJy (Vurm & Metzger 2021), which gives a detection horizon of only  $\sim 30$  Mpc for our fiducial SN/LGRB PWNe and 3 Mpc for our fiducial KN/SGRB PWNe. The Karl G. Jansky Very Large Array (VLA) and Atacama Large Millimeter/submillimeter Array (ALMA) have  $3\sigma$  detection limits of roughly 15 and 50  $\mu$ Jy for 1 and 100 GHz respectively (Omand et al. 2018; Eftekhari et al. 2021). Based on Figure 1, the detection horizon for our fiducial SN/LGRB PWNe is  $\sim 250$  Mpc ( $z \sim 0.06$ ) at 1 GHz and 200 Mpc ( $z \sim 0.05$ ) at 100 GHz, while for our fiducial KN/SGRB PWN the detection horizon is  $\sim 1.5$  Gpc ( $z \sim 0.3$ ) at 1 GHz and 1.0 Gpc ( $z \sim 0.2$ ) at 100 GHz. The horizon for SNe/LGRBs is lower than almost all Ic-BL SNe (Taddia et al. 2019; Srinivasaragavan et al. 2024) and LGRBs (Horvath et al. 2022), however, the horizon for KNe/SGRBs contains roughly 10% of the SGRB distribution (Ghirlanda et al. 2016). Schroeder et al. (2020) observed several  $z < 0.5$  SGRBs at 6 GHz around 2 – 14 years post-burst and did not detect any emission, placing constraints on both the PWN and ejecta afterglow emission.

Next-generation radio telescopes, such as DSA-2000 and ngVLA will have  $3\sigma$  detection limits of  $\sim 1 \mu$ Jy in the 1 – 100 GHz bands (Hallinan et al. 2019; McKinnon et al. 2019; Di Francesco et al. 2019), giving horizons of  $\sim 1 - 1.5$  Gpc ( $z \sim 0.2 - 0.3$ ) for our fiducial SN/LGRB PWNe and  $\sim 4 - 10$  Gpc ( $z \sim 0.7 - 1.5$ ) for our fiducial KN/SGRB PWNe. Most classified Ic-BL SNe are detected below the SNe/LGRB horizon (Taddia et al. 2019; Srinivasaragavan et al. 2024), although the majority of LGRBs are at higher redshifts (Lan et al. 2021). The horizon for SGRBs comprises around 50% of the population at 1 GHz and almost the entire population at 100 GHz (Ghirlanda et al. 2016).

We precluded modeling of the optical/UV signal due to possible contamination from the associated SN/KN. The absorption processes for optical/UV emission are primarily bound-bound transitions that thermalize the energy in the ejecta, and the escape timescale is thus given by the nebular timescale for the ejecta. For typical GRB-SNe, this timescale is around 1 – 2 months, while for magnetar-driven KNe, this timescale is around 1 – 5 days. Models of these transients predict strong optical emission at these times (Sarin et al. 2022; Omand & Sarin 2024), although near-UV emission can decline sharply as the transient cools, leaving a window for the non-thermal emission to be detectable at these wavelengths.

Given the need for well-timed, high-cadence, multi-band observations to confirm this scenario, it's important to note the early signals of magnetar-driven GRBs. This is especially important to coordinate facilities like ALMA, which can take as long as two weeks to respond to a target-of-opportunity trigger<sup>3</sup>, which is comparable to the escape timescale at 100 GHz in the fiducial KN/SGRB. With the horizons calculated above, it is unlikely we will detect PWN emission for all but the closest LGRBs or for SGRBs above  $z \approx 0.3$  with current instruments, so it is best to focus on low-redshift SGRBs. Early signals typically associated with the presence of a central magnetar are x-ray plateaus (Rowlinson et al. 2013; Gompertz et al. 2014; Stratta et al. 2018; Sarin et al. 2020a) and extended emission (Metzger et al. 2008; Bucciantini et al. 2012; Gompertz et al. 2013, 2014; Gibson et al. 2017; Sarin et al. 2020b). For closer objects, a gravitational wave detection of a binary neutron star merger coincident with the GRB showing a low chirp mass and an anomalously bright kilonova (Yu et al. 2013; Metzger 2019; Sarin et al. 2022; Ai et al. 2024), would mark it as a strong candidate for being magnetar-powered. Binary neutron star mergers are also expected to be neutrino sources on a short timescale (Kyotoku & Kashiyama 2018), but a long-lived

<sup>3</sup> <https://almascience.eso.org/observing/too-activation>

magnetar remnant could emit neutrinos on a longer timescale due to the interaction of the hadrons in the pulsar wind and ejecta (Bednarek 2003; Di Palma et al. 2017).

Modeling the three different emission components and their interactions is extremely difficult, and our simplified treatment of the non-thermal emission components has a few notable caveats. The PWN and transient ejecta are assumed to be spherical in this model, although in reality this symmetry can be broken in plenty of ways. Most numerical simulations of kilonovae show large deviations from spherical symmetry (Bauswein et al. 2013; Hotokezaka et al. 2013; Rosswog et al. 2014), and interaction between the jet and ejecta can cause the geometry and emission of both to be affected (Nativi et al. 2021, 2022). The PWN can be aspherical due to Kelvin-Helmholtz instabilities, and the nebula can also cause strong Rayleigh-Taylor instabilities within the transient ejecta, which can form ejecta filaments (Davidson & Fesen 1985; Jun 1998; Bucciantini et al. 2004; Porth et al. 2014) and cause the PWN forward shock to break out of the material (Blondin & Chevalier 2017; Suzuki & Maeda 2017; Omand et al. 2024). The rebrightenings could also be caused by more complicated jet geometries and afterglow physics, such as an exotic jet shape (Takahashi & Ioka 2021; Beniamini et al. 2022), counterjet (Granot & Loeb 2003; Li & Song 2004; Wang et al. 2009; Zhang & MacFadyen 2009; Ghosh Dastidar & Duffell 2024), reverse shock (Kobayashi et al. 1999; Kobayashi & Sari 2000; Uhm et al. 2012), or late energy injection into the shock, causing a refreshed shock (Rees & Mészáros 1998; Panaiteescu et al. 1998; Zhang & Mészáros 2002). The GRB and ejecta afterglow models we use both assume the surrounding medium has constant density, which is not true in the case of wind or eruptive mass loss from the progenitor. The top-hat model also ignores the effects of the magnetar on the jet itself, which could produce an x-ray plateau in the early afterglow (Rowlinson et al. 2013; Gompertz et al. 2014; Stratta et al. 2018). The use of a one-zone spherical ejecta afterglow also neglects the effects of the density structure of the ejecta, which can cause over an order of magnitude difference in the observed signal (Rosswog et al. 2024).

The parameters used for the microphysics of our fiducial PWN are consistent with that of Galactic PWNe such as the Crab (Tanaka & Takahara 2010, 2013), the lack of observed radio counterparts (Law et al. 2019; Eftekhari et al. 2021) shows that this assumption may not be correct for most magnetar-driven supernovae. A couple of alternate microphysical models are the high-magnetization PWN model (Murase et al. 2021), where the synchrotron energy peaks in the MeV range, and the low-magnetization model (Vurm & Metzger 2021), where the emission is dominated by inverse-Compton emission ( $Y_{\text{IC}} \gtrsim 10$ ). The latter of these models is also motivated by strong non-thermal losses in SLSNe (Vurm & Metzger 2021).

Our model does not include inverse-Compton emission for simplicity, but we can examine the high-magnetization model further. Figure 3 shows the 100 keV light curves for our fiducial SN/LGRB and KN/SGRB with  $\epsilon_{\text{B,PWN}} = 0.5$ ,  $\gamma_b = 10^7$ , and the low-energy spectral index  $q_1 = 1$ , as used in Murase et al. (2021). The PWN signal at 100 keV for both types of objects is lower than the cases with Crab-like microphysics due to the peak of the spectrum being in the 10 – 100 MeV range and the steeper spectral index. This is consistent with Vurm & Metzger (2021) and Murase et al. (2021), which show the two models having emission of around the same order of magnitude at 100 keV. Those studies also show that detecting the emission at  $> 1$  MeV will likely require next generation instruments, such as eASTROGAM and AMEGO. While it may be possible to have a synchrotron spectrum that peaks at  $\sim 100$  keV around the PWN escape time, such a model would likely need to be fine-tuned and require more physical motivation.

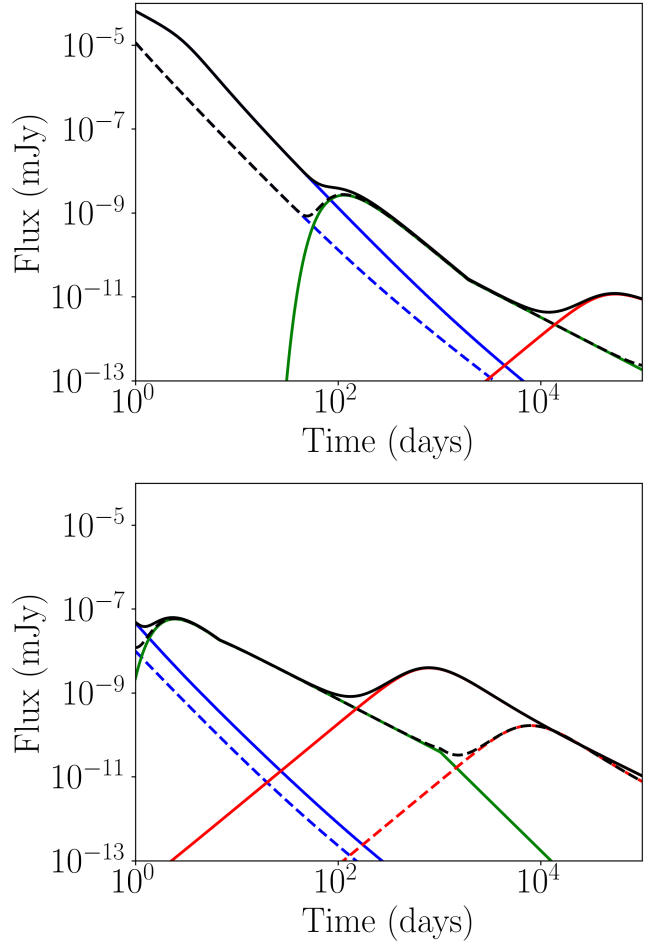


**Figure 3.** 100 keV light curves for magnetar-driven supernovae and kilonovae with an on-axis GRB and a high-magnetization PWN. Each panel shows the GRB afterglow (blue), PWN (green), ejecta afterglow (red), and total emission (black). The solid and dashed lines indicate the density of the ambient medium  $n_{\text{CSM}}$  to be 1 and  $10^{-3} \text{ cm}^{-3}$  respectively.

The SGRB counterpart to the binary neutron star (BNS) merger GW170817, GRB170817A, is the closest SGRB to date (Fong et al. 2022; Nugent et al. 2022) and one of the most studied transients in history (e.g., Abbott et al. 2017a,b,c; Margutti & Chornock 2021). The total mass of the BNS system was inferred to be  $\sim 2.7 M_{\odot}$  (Abbott et al. 2019) with  $< 0.1 M_{\odot}$  of ejected material, which is larger than the inferred maximum non-rotating neutron star mass  $M_{\text{TOV}}$  of  $2.2 - 2.3 M_{\odot}$ . However, several studies propose that GW170817 could have had a long-lived or infinitely stable neutron star, especially if the spin-down luminosity is dominated by gravitational wave emission (Ai et al. 2018; Yu et al. 2018; Piro et al. 2019; Sarin & Lasky 2021; DuPont & MacFadyen 2024). Figure 4 shows the afterglow of GRB170817A in optical, x-ray, and radio (Evans et al. 2017; Hallinan et al. 2017; Haggard et al. 2017; Mooley et al. 2018; Lyman et al. 2018), along with a Gaussian jet light curve model using the median parameters from Lamb et al. (2019a). We note that the afterglow models used here and in Lamb et al. (2019a) have slightly different physics, and thus our model does not match the data exactly. We show a GRB afterglow without a PWN and two with initial magnetar luminosities of  $L_0 = 10^{50}$  ( $E_{\text{rot}} = 10^{52}$ ) and  $L_0 = 10^{49}$  ( $E_{\text{rot}} = 10^{51}$ ), with all other parameters being taken from the fiducial case. With a

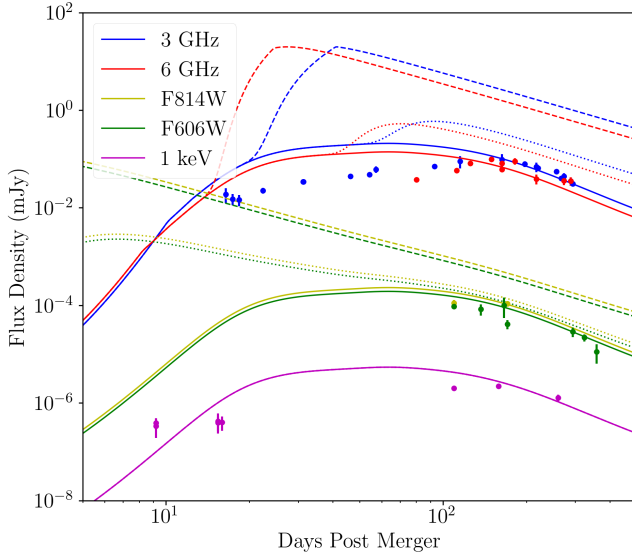


**Figure 4.** The GRB afterglow of GRB170817A in optical, x-ray, and radio (Evans et al. 2017; Hallinan et al. 2017; Haggard et al. 2017; Mooley et al. 2018) and a Gaussian jet light curve model using the median parameters from Lamb et al. (2019a). PWNe from magnetars with  $L_0 = 10^{50}$  ( $E_{\text{rot}} = 10^{52}$ ) and  $L_0 = 10^{49}$  ( $E_{\text{rot}} = 10^{51}$ ) are shown with dashed and dotted lines, respectively, while the afterglow with no PWN is shown with solid lines. The other PWN parameters are taken from the fiducial KN/SGRB case.

PWN, both the optical and radio emission are significantly more luminous than observed, and the radio emission shows a distinctive rise at around  $10 - 100$  days, which would have been readily observable. The optical emission would have also risen on the timescale of  $1 - 2$  days and would have been detectable in the initial kilonova emission. This shows that if the remnant of the 170817 BNS merger is a stable neutron star, the rotational energy of the neutron star emitted in electromagnetic radiation would have to be  $\lesssim 10^{51}$  erg in order to not be detectable in the afterglow, which gives a conservative lower limit on the initial spin period of  $\sim 7$  ms for a  $2.2 M_\odot$  neutron star.

A recent case is GRB210702A, which showed a frequency-dependent rebrightening as predicted by the PWN model (de Wet et al. 2024). However, GRB210702A is an LGRB at  $z = 1.160$  (Xu et al. 2021) with the rebrightening starting at  $\sim 10$  days in the observer frame, bringing the rest frame rebrightening time to  $\sim 5$  days. Given the timescale from Equation 5, this would require  $\lesssim 0.01 M_\odot$  of ejecta traveling at a significant fraction of the speed of light, which is unrealistic for even a kilonova. The distance is also far outside the expected horizon for our fiducial parameters, so the effect of the PWN would be difficult to observe in this object. Thus, it seems unlikely that the source of the rebrightening could be a PWN.

## 5 SUMMARY

Non-thermal light curves from magnetar-powered GRBs can show emission from the GRB afterglow, PWN, and ejecta afterglow. The timescales for the peak of each emission component are different in both radio and x-ray for our fiducial parameters, making each component potentially distinguishable in the resulting light curve. The GRB afterglow will peak first, followed by the PWN, then the ejecta afterglow. The GRB and ejecta afterglow peak timescales are set by the deceleration timescale and the movement of the spectral peak

across the band, while the PWN peak timescale is set by absorption processes within the transient ejecta, giving different behaviours across different bands for the peak timescales.

We show the light curves for fiducial SNe/LGRBs and KNe/SGRBs, both on- and off-axis, at 1 GHz, 100 GHz, 1 keV, and 100 keV. At 1 GHz, the PWN dominates the emission at  $\sim 6$  years for SNe/LGRBs and  $\sim 100$  days for KN/SGRBs, although PWN can be subdominant to a KN afterglow if the density of the surrounding medium is high enough. At 100 GHz, the PWN dominates the emission at  $\sim 1$  year for SNe/LGRBs and  $\sim 15$  days for KN/SGRBs, regardless of the density of the ambient medium. The PWN will never be detectable at 1 keV due to strong absorption, and while the PWN does dominate the 100 keV emission over the first few decades, the emission is faint enough that detecting it with current instruments is impossible.

We simulate our fiducial KN/SGRB observed at 1 and 100 GHz and fit it with a three-component model using a prior that can effectively turn off the PWN component. The posterior shows a 0% probability that the transient can be explained without a PWN component. The two distinguishing features of the PWN component are the frequency-dependent rise and the fast rise from only afterglow emission to PWN peak. The ejecta afterglow can show a frequency-dependent rise time in atypical cases, but the rise will slow down in those cases, making it possible to distinguish through high-cadence observations.

The detection horizon for the fiducial PWN in these scenarios is  $z \sim 0.05 - 0.06$  for SN/LGRBs and  $z \sim 0.2 - 0.3$  for KN/SGRBs with current instruments and  $z \sim 0.2 - 0.3$  for SN/LGRBs and  $z \sim 0.7 - 1.5$  for KN/SGRBs with next-generation instruments. The PWN emission would be detectable in optical, but will likely compete with the thermal emission from the transient. Our simple treatment of the emission components neglects asymmetry and interaction between the different components, which can have a strong effect but is difficult to describe in a self-consistent way. We modeled the potential non-thermal emission from GRB170817A and GRB210702A and found that neither of them are likely to contain a PWN. The optimal observing strategy for detecting PWNe in GRB afterglows is multi-band, high-cadence radio follow-up from  $10 - 100$  days of nearby SGRBs with an x-ray plateau or extended emission.

## ACKNOWLEDGEMENTS

The authors thank Simon de Wet for sharing the data for GRB210702A, and Shiho Kobayashi and Cairns Turnbull for helpful discussions. C. M. B. O. and G. P. L. acknowledge support from the Royal Society (grant Nos. DHF-R1-221175 and DHF-ERE-221005). N. S. acknowledges support from the Knut and Alice Wallenberg foundation through the “Gravity Meets Light” project.

## DATA AVAILABILITY

The models are available for public use within REDBACK (Sarin et al. 2024).

## REFERENCES

- Abbott B. P., Abbott R., Abbott T. D., et al. 2017a, *ApJ*, **848**, L12
- Abbott B. P., Abbott R., Abbott T. D., et al. 2017b, *ApJ*, **848**, L13
- Abbott B. P., Abbott R., Abbott T. D., et al. 2017c, *ApJ*, **850**, L39

- Abbott B. P., Abbott R., Abbott T. D., et al. 2019, *Physical Review X*, **9**, 011001
- Abbott B. P., Abbott R., Abbott T. D., et al. 2020, *Living Reviews in Relativity*, **23**, 3
- Ai S., Gao H., Dai Z.-G., et al. 2018, *ApJ*, **860**, 57
- Ai S., Gao H., Zhang B., 2024, *arXiv e-prints*, p. arXiv:2405.00638
- Ashton G., Hübner M., Lasky P. D., et al. 2019, *ApJS*, **241**, 27
- Atteia J. L., Heussaff V., Dezalay J. P., et al. 2017, *ApJ*, **837**, 119
- Bauswein A., Goriely S., Janka H. T., 2013, *ApJ*, **773**, 78
- Bednarek W., 2003, *A&A*, **407**, 1
- Beniamini P., Gill R., Granot J., 2022, *MNRAS*, **515**, 555
- Bietenholz M. F., Kronberg P. P., Hogg D. E., et al. 1991, *ApJ*, **373**, L59
- Blandford R. D., McKee C. F., 1976, *Physics of Fluids*, **19**, 1130
- Blandford R. D., McKee C. F., 1977, *MNRAS*, **180**, 343
- Blandford R. D., Payne D. G., 1982, *MNRAS*, **199**, 883
- Blandford R. D., Znajek R. L., 1977, *MNRAS*, **179**, 433
- Blinnikov S. I., Novikov I. D., Perevodchikova T. V., et al. 1984, *Soviet Astronomy Letters*, **10**, 177
- Blondin J. M., Chevalier R. A., 2017, *ApJ*, **845**, 139
- Bochenek C. D., Dwarkadas V. V., Silverman J. M., et al. 2018, *MNRAS*, **473**, 336
- Bostancı Z. F., Kaneko Y., Göögüs E., 2013, *MNRAS*, **428**, 1623
- Bucciantini N., Amato E., Bandiera R., et al. 2004, *A&A*, **423**, 253
- Bucciantini N., Metzger B. D., Thompson T. A., et al. 2012, *MNRAS*, **419**, 1537
- Buchner J., Georgakakis A., Nandra K., et al. 2014, *A&A*, **564**, A125
- Bugli M., Guilet J., Obergaullinger M., 2021, *MNRAS*, **507**, 443
- Cano Z., Wang S.-Q., Dai Z.-G., et al. 2017, *Advances in Astronomy*, **2017**, 8929054
- Chen K.-J., Woosley S. E., Sukhbold T., 2016, *ApJ*, **832**, 73
- Chen T. W., Brennan S. J., Wesson R., et al. 2021, *arXiv e-prints*, p. arXiv:2109.07942
- Chevalier R. A., Fransson C., 1992, *ApJ*, **395**, 540
- Chevalier R. A., Fransson C., 1994, *ApJ*, **420**, 268
- Clark D. H., Murdin P., Wood R., et al. 1983, *MNRAS*, **204**, 415
- Corsi A., Ho A. Y. Q., Cenko S. B., et al. 2022, *arXiv e-prints*, p. arXiv:2210.09536
- Dainotti M. G., Nagataki S., Maeda K., et al. 2017, *A&A*, **600**, A98
- Davidson K., Fesen R. A., 1985, *ARA&A*, **23**, 119
- Dessart L., 2024, *arXiv e-prints*, p. arXiv:2408.13844
- Di Francesco J., Chalmers D., Denman N., et al. 2019, in Canadian Long Range Plan for Astronomy and Astrophysics White Papers. p. 32 (arXiv:1911.01517), doi:10.5281/zenodo.3765763
- Di Palma I., Guetta D., Amato E., 2017, *ApJ*, **836**, 159
- Drouet M. R., Milisavljevic D., Parrent J., et al. 2016, *ApJ*, **821**, 57
- DuPont M., MacFadyen A., 2024, *ApJ*, **971**, L24
- Duncan R. C., Thompson C., 1992, *ApJ*, **392**, L9
- Dwarkadas V. V., 2014, *MNRAS*, **440**, 1917
- Eftekhari T., Berger E., Margalit B., et al. 2019, *ApJ*, **876**, L10
- Eftekhari T., Margalit B., Omand C. M. B., et al. 2021, *ApJ*, **912**, 21
- Eichler D., Livio M., Piran T., et al. 1989, *Nature*, **340**, 126
- Evans P. A., Cenko S. B., Kennea J. A., et al. 2017, *Science*, **358**, 1565
- Fong W., Berger E., Margutti R., et al. 2015, *ApJ*, **815**, 102
- Fong W., et al., 2021, *ApJ*, **906**, 127
- Fong W.-f., Nugent A. E., Dong Y., et al. 2022, *ApJ*, **940**, 56
- Foucart F., Haas R., Duez M. D., et al. 2016, *Phys. Rev. D*, **93**, 044019
- Fransson C., Ergon M., Challis P. J., et al. 2014, *ApJ*, **797**, 118
- Gaensler B. M., Manchester R. N., Staveley-Smith L., et al. 1997, *ApJ*, **479**, 845
- Gehrels N., Mészáros P., 2012, *Science*, **337**, 932
- Gendre B., Stratta G., Atteia J. L., et al. 2013, *ApJ*, **766**, 30
- Ghirlanda G., Salafia O. S., Pescalli A., et al. 2016, *A&A*, **594**, A84
- Ghosh Dastidar R., Duffell P., 2024, *arXiv e-prints*, p. arXiv:2410.12185
- Gibson S. L., Wynn G. A., Gompertz B. P., et al. 2017, *MNRAS*, **470**, 4925
- Gkini A., Lunnar N., Schulze S., et al. 2024, *A&A*, **685**, A20
- Gomez S., Nicholl M., Berger E., et al. 2024, *arXiv e-prints*, p. arXiv:2407.07946
- Gompertz B. P., O'Brien P. T., Wynn G. A., et al. 2013, *MNRAS*, **431**, 1745
- Gompertz B. P., O'Brien P. T., Wynn G. A., 2014, *MNRAS*, **438**, 240
- Granot J., Loeb A., 2003, *ApJ*, **593**, L81
- Granot J., Panaiteescu A., Kumar P., Woosley S. E., 2002, *ApJ*, **570**, L61
- Greiner J., Mazzali P. A., Kann D. A., et al. 2015, *Nature*, **523**, 189
- Haggard D., Nynka M., Ruan J. J., et al. 2017, *ApJ*, **848**, L25
- Hajela A., Margutti R., Bright J. S., et al. 2022, *ApJ*, **927**, L17
- Hallinan G., Corsi A., Mooley K. P., et al. 2017, *Science*, **358**, 1579
- Hallinan G., Ravi V., Weinreb S., et al. 2019, in *Bulletin of the American Astronomical Society*. p. 255 (arXiv:1907.07648), doi:10.48550/arXiv.1907.07648
- Horvath I., Racz I. I., Bagoly Z., et al. 2022, *Universe*, **8**, 221
- Hotokezaka K., Kiuchi K., Kyutoku K., et al. 2013, *Phys. Rev. D*, **87**, 024001
- Hotokezaka K., Nissanke S., Hallinan G., et al. 2016, *ApJ*, **831**, 190
- Hotokezaka K., Tanaka M., Kato D., et al. 2021, *MNRAS*, **506**, 5863
- Illarionov A. F., Sunyaev R. A., 1975, *A&A*, **39**, 185
- Inserra C., Bulla M., Sim S. A., et al. 2016, *ApJ*, **831**, 79
- Ioka K., Nakamura T., 2018, *Progress of Theoretical and Experimental Physics*, **2018**, 043E02
- Jerkstrand A., Smartt S. J., Inserra C., et al. 2017, *ApJ*, **835**, 13
- Jin Z.-P., et al., 2016, *Nature Communications*, **7**, 12898
- Jin Z.-P., Covino S., Liao N.-H., Li X., D'Avanzo P., Fan Y.-Z., Wei D.-M., 2020, *Nature Astronomy*, **4**, 77
- Jun B.-I., 1998, *ApJ*, **499**, 282
- Kaneko Y., Bostancı Z. F., Göögüs E., et al. 2015, *MNRAS*, **452**, 824
- Kangas T., Yan L., Schulze S., et al. 2022, *MNRAS*, **516**, 1193
- Kashiyama K., Murase K., Bartos I., et al. 2016, *ApJ*, **818**, 94
- Kennel C. F., Coroniti F. V., 1984, *ApJ*, **283**, 694
- Klein O., Nishina T., 1929, *Zeitschrift fur Physik*, **52**, 853
- Kobayashi S., Sari R., 2000, *ApJ*, **542**, 819
- Kobayashi S., Piran T., Sari R., 1999, *ApJ*, **513**, 669
- Kool E. C., Johansson J., Sollerman J., et al. 2023, *Nature*, **617**, 477
- Kouveliotou C., Meegan C. A., Fishman G. J., et al. 1993, *ApJ*, **413**, L101
- Kyutoku K., Kashiyama K., 2018, *Phys. Rev. D*, **97**, 103001
- Lamb G. P., Kobayashi S., 2017, *MNRAS*, **472**, 4953
- Lamb G. P., Mandel I., Resmi L., 2018, *MNRAS*, **481**, 2581
- Lamb G. P., Lyman J. D., Levan A. J., et al. 2019a, *ApJ*, **870**, L15
- Lamb G. P., et al., 2019b, *ApJ*, **883**, 48
- Lan G.-X., Wei J.-J., Zeng H.-D., et al. 2021, *MNRAS*, **508**, 52
- Lang K. R., 1999, *Astrophysical formulae*
- Lasky P. D., Leris C., Rowlinson A., et al. 2017, *ApJ*, **843**, L1
- Lattimer J. M., Schramm D. N., 1976, *ApJ*, **210**, 549
- Law C. J., Omand C. M. B., Kashiyama K., et al. 2019, *ApJ*, **886**, 24
- Levan A. J., Tanvir N. R., Starling R. L. C., et al. 2014, *ApJ*, **781**, 13
- Levan A. J., Gompertz B. P., Salafia O. S., et al. 2024, *Nature*, **626**, 737
- Li Z., Song L. M., 2004, *ApJ*, **614**, L17
- Lovelace R. V. E., Romanova M. M., Bisnovatyi-Kogan G. S., 1999, *ApJ*, **514**, 368
- Lyman J. D., Lamb G. P., Levan A. J., et al. 2018, *Nature Astronomy*, **2**, 751
- MAGIC Collaboration Acciari V. A., Ansoldi S., et al. 2019, *Nature*, **575**, 459
- MacFadyen A. I., Woosley S. E., 1999, *ApJ*, **524**, 262
- MacFadyen A. I., Woosley S. E., Heger A., 2001, *ApJ*, **550**, 410
- Malsiner-Walli G., Wagner H., 2018, *arXiv e-prints*, p. arXiv:1812.07259
- Margalit B., Metzger B. D., 2019, *ApJ*, **880**, L15
- Margalit B., Piran T., 2020, *MNRAS*, **495**, 4981
- Margutti R., Chornock R., 2021, *ARA&A*, **59**, 155
- Margutti R., Bright J. S., Matthews D. J., et al. 2023, *ApJ*, **954**, L45
- Mazzali P. A., MacFadyen A. I., Woosley S. E., et al. 2014, *MNRAS*, **443**, 67
- McKinnon M., Beasley A., Murphy E., et al. 2019, in *Bulletin of the American Astronomical Society*. p. 81
- Mészáros P., 2006, *Reports on Progress in Physics*, **69**, 2259
- Metzger B. D., 2019, *Living Reviews in Relativity*, **23**, 1
- Metzger B. D., Quataert E., Thompson T. A., 2008, *MNRAS*, **385**, 1455
- Mondal S., Bera A., Chandra P., et al. 2020, *MNRAS*, **498**, 3863
- Mooley K. P., Nakar E., Hotokezaka K., et al. 2018, *Nature*, **554**, 207
- Mösta P., Radice D., Haas R., et al. 2020, *ApJ*, **901**, L37
- Murase K., Kashiyama K., Kiuchi K., et al. 2015, *ApJ*, **805**, 82
- Murase K., Kashiyama K., Mészáros P., 2017, *MNRAS*, **467**, 3542

- Murase K., Omand C. M. B., Coppejans D. L., et al. 2021, *MNRAS*, **508**, 44  
 Nakar E., Piran T., 2011, *Nature*, **478**, 82  
 Nakar E., Piran T., Granot J., 2002, *ApJ*, **579**, 699  
 Nakauchi D., Kashiyama K., Suwa Y., et al. 2013, *ApJ*, **778**, 67  
 Nativi L., Bulla M., Rosswog S., et al. 2021, *MNRAS*, **500**, 1772  
 Nativi L., Lamb G. P., Rosswog S., et al. 2022, *MNRAS*, **509**, 903  
 Nicholl M., Guillochon J., Berger E., 2017, *ApJ*, **850**, 55  
 Norris J. P., Bonnell J. T., 2006, *ApJ*, **643**, 266  
 Nousek J. A., Kouveliotou C., Grupe D., et al. 2006, *ApJ*, **642**, 389  
 Nugent A. E., Fong W.-F., Dong Y., et al. 2022, *ApJ*, **940**, 57  
 O'Brien P. T., Willingale R., Osborne J., et al. 2006, *ApJ*, **647**, 1213  
 Omand C. M. B., Jerkstrand A., 2023, *A&A*, **673**, A107  
 Omand C. M. B., Sarin N., 2024, *MNRAS*, **527**, 6455  
 Omand C. M. B., Kashiyama K., Murase K., 2018, *MNRAS*, **474**, 573  
 Omand C. M. B., Kashiyama K., Murase K., 2019, *MNRAS*, **484**, 5468  
 Omand C. M. B., Sarin N., Temim T., 2024, arXiv e-prints, p. arXiv:2404.19017  
 Paczynski B., Rhoads J. E., 1993, *ApJ*, **418**, L5  
 Panaiteescu A., Mészáros P., Rees M. J., 1998, *ApJ*, **503**, 314  
 Piran T., 2004, *Reviews of Modern Physics*, **76**, 1143  
 Piro L., Troja E., Zhang B., et al. 2019, *MNRAS*, **483**, 1912  
 Pognan Q., Grumer J., Jerkstrand A., et al. 2023, *MNRAS*, **526**, 5220  
 Poidevin F., Omand C. M. B., Pérez-Fournon I., et al. 2022, *MNRAS*, **511**, 5948  
 Poidevin F., Omand C. M. B., Könyves-Tóth R., et al. 2023, *MNRAS*, **521**, 5418  
 Popham R., Woosley S. E., Fryer C., 1999, *ApJ*, **518**, 356  
 Porth O., Komissarov S. S., Keppens R., 2014, *MNRAS*, **443**, 547  
 Pursiainen M., Leloudas G., Paraskeva E., et al. 2022, *A&A*, **666**, A30  
 Pursiainen M., Leloudas G., Cikota A., et al. 2023, *A&A*, **674**, A81  
 Rastinejad J. C., Gompertz B. P., Levan A. J., et al. 2022, *Nature*, **612**, 223  
 Rees M. J., Mészáros P., 1998, *ApJ*, **496**, L1  
 Roberts L. F., Lippuner J., Duez M. D., et al. 2017, *MNRAS*, **464**, 3907  
 Romanova M. M., Ustyugova G. V., Koldoba A. V., et al. 2005, *ApJ*, **635**, L165  
 Rossi E., Lazzati D., Rees M. J., 2002, *MNRAS*, **332**, 945  
 Rosswog S., Korobkin O., Arcones A., et al. 2014, *MNRAS*, **439**, 744  
 Rosswog S., Diener P., Torsello F., et al. 2024, *MNRAS*, **530**, 2336  
 Rowlinson A., O'Brien P. T., Metzger B. D., et al. 2013, *MNRAS*, **430**, 1061  
 Saito S., Tanaka M., Moriya T. J., et al. 2020, *ApJ*, **894**, 154  
 Sari R., Piran T., Narayan R., 1998, *ApJ*, **497**, L17  
 Sarin N., Lasky P. D., 2021, *General Relativity and Gravitation*, **53**, 59  
 Sarin N., Lasky P. D., Ashton G., 2019, *ApJ*, **872**, 114  
 Sarin N., Lasky P. D., Ashton G., 2020a, *Phys. Rev. D*, **101**, 063021  
 Sarin N., Lasky P. D., Ashton G., 2020b, *MNRAS*, **499**, 5986  
 Sarin N., Omand C. M. B., Margalit B., et al. 2022, *MNRAS*, **516**, 4949  
 Sarin N., Hübner M., Omand C. M. B., Setzer C. N., et al. 2024, *MNRAS*, **531**, 1203  
 Schroeder G., Margalit B., Fong W.-f., et al. 2020, *ApJ*, **902**, 82  
 Schutz B. F., 2011, *Classical and Quantum Gravity*, **28**, 125023  
 Siegel D. M., Metzger B. D., 2017, *Phys. Rev. Lett.*, **119**, 231102  
 Smith N., Chornock R., Li W., et al. 2008, *ApJ*, **686**, 467  
 Srinivasaragavan G. P., Yang S., Anand S., et al. 2024, arXiv e-prints, p. arXiv:2408.14586  
 Stratta G., Dainotti M. G., Dall'Osso S., et al. 2018, *ApJ*, **869**, 155  
 Sun L., Xiao L., Li G., 2022, *MNRAS*, **513**, 4057  
 Suzuki A., Maeda K., 2017, *MNRAS*, **466**, 2633  
 Suzuki A., Maeda K., 2021, *ApJ*, **908**, 217  
 Taddia F., Sollerman J., Fremling C., et al. 2019, *A&A*, **621**, A71  
 Takahashi K., Ioka K., 2021, *MNRAS*, **501**, 5746  
 Tanaka S. J., Takahara F., 2010, *ApJ*, **715**, 1248  
 Tanaka S. J., Takahara F., 2013, *MNRAS*, **429**, 2945  
 Tanvir N. R., Levan A. J., Fruchter A. S., Hjorth J., Hounsell R. A., Wiersema K., Tunncliffe R. L., 2013, *Nature*, **500**, 547  
 Temim T., et al., 2006, *AJ*, **132**, 1610  
 Troja E., Cusumano G., O'Brien P. T., et al. 2007, *ApJ*, **665**, 599  
 Troja E., O'Connor B., Ryan G., et al. 2022, *MNRAS*, **510**, 1902  
 Uhm Z. L., Zhang B., Hascoët R., et al. 2012, *ApJ*, **761**, 147
- Vlasov A. D., Metzger B. D., Lippuner J., et al. 2017, *MNRAS*, **468**, 1522  
 Vurm I., Metzger B. D., 2021, *ApJ*, **917**, 77  
 Wang X., Huang Y. F., Kong S. W., 2009, *A&A*, **505**, 1213  
 Wang X.-G., Zhang B., Liang E.-W., et al. 2015, *ApJS*, **219**, 9  
 Wang L. J., Yu H., Liu L. D., et al. 2017, *ApJ*, **837**, 128  
 West S. L., Lunnan R., Omand C. M. B., et al. 2023, *A&A*, **670**, A7  
 Xie X., Zrake J., MacFadyen A., 2018, *ApJ*, **863**, 58  
 Xu D., Izzo L., de Ugarte Postigo A., et al. 2021, GRB Coordinates Network, **30357**, 1  
 Yang B., et al., 2015, *Nature Communications*, **6**, 7323  
 Yu Y.-W., Zhang B., Gao H., 2013, *ApJ*, **776**, L40  
 Yu Y.-W., Liu L.-D., Dai Z.-G., 2018, *ApJ*, **861**, 114  
 Zhang B., 2018, The Physics of Gamma-Ray Bursts, doi:10.1017/978139226530.  
 Zhang W., MacFadyen A., 2009, *ApJ*, **698**, 1261  
 Zhang B., Mészáros P., 2002, *ApJ*, **566**, 712  
 Zhang B., Mészáros P., 2004, *International Journal of Modern Physics A*, **19**, 2385  
 Zhang B., Fan Y. Z., Dyks J., et al. 2006, *ApJ*, **642**, 354  
 Zhou H., Jin Z.-P., Covino S., Lei L., An Y., Gong H.-Y., Fan Y.-Z., Wei D.-M., 2023, *ApJ*, **943**, 104  
 Zhu Y.-M., Zhou H., Wang Y., Liao N.-H., Jin Z.-P., Wei D.-M., 2023, *MNRAS*, **521**, 269  
 de Wet S., Laskar T., Groot P. J., et al. 2024, *ApJ*, **974**, 279  
 van Dyk S. D., Weiler K. W., Sramek R. A., et al. 1994, *ApJ*, **432**, L115

## APPENDIX A: OVERVIEW OF THE PWN MODEL

This model is based on the analytic scalings presented in Murase et al. (2021). The dynamics for the model are calculated in the same way as Sarin et al. (2022) and Omand & Sarin (2024); see those papers for details.

### A1 Emission

The spin-down luminosity of the PWN can be given by the equation (Lasky et al. 2017)

$$L_{\text{SD}}(t) = L_0 \left(1 + \frac{t}{t_{\text{SD}}}\right)^{\frac{1+n}{1-n}}, \quad (\text{A1})$$

where  $L_0$  is the initial PWN luminosity,  $t_{\text{SD}}$  is the spin-down time, and  $n$  is the pulsar breaking index. Equation A1 can be substituted for other spin-down formalisms, such as in Sarin et al. (2022). The magnetic field of the PWN is estimated as

$$B_{\text{neb}} \approx \sqrt{\frac{6\epsilon_B}{R_{\text{ej}}^3} \int L_{\text{SD}} dt}, \quad (\text{A2})$$

where  $\epsilon_B$  is the fraction of spin-down energy carried in the magnetic field of the PWN. This value is usually around 0.003 for Galactic PWNe (Kennel & Coroniti 1984; Tanaka & Takahara 2010, 2013), but has been inferred to be lower in some superluminous supernovae (Vurm & Metzger 2021). The characteristic synchrotron frequency, where  $\nu F_\nu$  peaks, is

$$\nu_b \approx \frac{3}{4\pi} \gamma_b^2 \frac{eB_{\text{neb}}}{m_e c}, \quad (\text{A3})$$

where  $\gamma_b$  is the electron injection Lorentz factor, usually taken to be  $10^4 - 10^7$  for Galactic PWNe (Tanaka & Takahara 2013). This is true if  $\nu_b$  is lower than the maximum synchrotron frequency  $\nu_M \sim 3.8 \times 10^{22}$  Hz.  $F_\nu$  in the fast cooling limit is

$$F_\nu = F_{\nu 0} \left(\frac{\nu}{\nu_0}\right)^{1-\beta_I} = \frac{\epsilon_e L_{\text{SD}}}{8\pi d^2 \nu_0 \mathcal{R}_0 (1+Y_{\text{IC}})} \left(\frac{\nu}{\nu_0}\right)^{1-\beta_I}, \quad (\text{A4})$$

for  $l = 1(2)$  when  $\nu < (>) \nu_0$ , where  $\nu_0 = \min[\nu_b, \nu_M]$  is the peak of the  $\nu F_\nu$  spectrum,  $\epsilon_e \approx 1 - \epsilon_B$  is the fraction of spin-down energy carried by non-thermal leptons,

$$\mathcal{R}_0 = \frac{1}{2 - q_1} - \frac{1}{2 - q_2} \quad (\text{A5})$$

is the bolometric normalization factor,  $Y_{\text{IC}}$  is the Compton  $Y$  parameter (which we assume to be 0, since we only model a synchrotron nebula), and  $d$  is the distance to the source. The photon indices  $\beta_1$  and  $\beta_2$  introduced by  $F_\nu \propto \nu^{1-\beta_n}$  are  $\beta_1 = \max[3/2, (2 + q_1)/2]$  and  $\beta_2 = (2 + q_2)/2$ , where  $q_1 < 2$  and  $q_2 > 2$  are the low and high energy spectral indices are the non-thermal leptons.

## A2 Absorption

PWN emission can be subject to various absorption processes depending on the frequency of the emission. At radio frequencies, synchrotron self-absorption (SSA) and free-free absorption (FFA) are the main processes. At 10 eV – 10 keV bands, the dominant process is photoelectric (bound-free) absorption. At 10 keV – 10 MeV bands, the dominant process is Compton scattering. Other bands have different processes, such as Bethe-Heitler pair production for  $> 10$  MeV bands and bound-bound absorption in the optical/infrared bands (Kashiyama et al. 2016), but we only include absorption processes in the radio and 10 eV – 10 MeV bands.

The SSA frequency can be estimated by (Murase et al. 2021)

$$\pi \frac{R_{\text{ej}}^2}{d^2} 2kT_{\text{ssa}} \frac{\nu_{\text{ssa}}^2}{c^2} = F_{\nu 0} \left( \frac{\nu_{\text{ssa}}}{\nu_0} \right)^{1-\beta_1}, \quad (\text{A6})$$

where

$$T_{\text{ssa}} = \frac{1}{3k} \left( \frac{4\pi m_e c \nu_{\text{ssa}}}{3e B_{\text{neb}}} \right)^{1/2} m_e c^2 \quad (\text{A7})$$

is the brightness temperature at  $T_{\text{ssa}}$ . This approximately gives

$$\nu_{\text{ssa}} \approx \left( \frac{3^{3/2} e^{1/2} B_{\text{neb}}^{1/2} F_{\nu 0} \nu_0^{\beta_1-1} d^2}{4\pi^{3/2} m_e^{3/2} c^{1/2} R_{\text{ej}}^2} \right)^{\frac{2}{2\beta_1+3}}. \quad (\text{A8})$$

The optical depth for free-free absorption is (Lang 1999; Murase et al. 2017)

$$\tau_{\text{ff}} \approx 8.4 \times 10^{-28} n_e^2 R_{\text{ej}} \bar{Z}^2 \left( \frac{\nu}{10 \text{ GHz}} \right)^{-2.1}, \quad (\text{A9})$$

where

$$n_e = \frac{3}{4\pi R_{\text{ej}}^3} \frac{M_{\text{ej}} Y_{\text{fe}}}{m_p} \quad (\text{A10})$$

is the electron density,  $\bar{Z}$  is the average atomic number of the ejected material, and

$$Y_{\text{fe}} \equiv \frac{n_{\text{fe}}}{n_p + n_n} \quad (\text{A11})$$

is the free electron fraction, with  $n_{\text{fe}}$  being the free electron density.

The optical depths for x-ray absorption can be generally written as  $\tau = \kappa \rho_{\text{ej}} R_{\text{ej}}$  for opacity  $\kappa$ , where the opacity for photoelectric absorption is approximated as (Murase et al. 2015; Kashiyama et al. 2016)

$$\kappa_{\text{pe}} = 11 \left( \frac{\bar{Z}}{10} \right)^3 \left( \frac{h\nu}{10 \text{ keV}} \right)^{-3} \text{ cm}^2 \text{ g}^{-1} \quad (\text{A12})$$

and for Compton scattering as (Murase et al. 2015)

$$\kappa_{\text{comp}} = \frac{\sigma_{\text{KN}} Y_e}{m_p}, \quad (\text{A13})$$

where  $\sigma_{\text{KN}}$  is the Klein-Nishina cross section (Klein & Nishina 1929) and  $Y_e$  is the electron fraction of the ejecta.

## A3 Parameters and Default Priors

This model is implemented as the PWN model in GENERAL\_SYNCHROTRON\_MODELS within REDBACK. Along with the parameters that can freely vary during inference, there are a number of parameters that have default values consistent with a supernova, but that can be changed if the user wants to model a kilonova. These can also be given priors and marginalized over if needed. The parameters  $\kappa$  and  $\kappa_\gamma$  here are only used in the dynamics on the supernova, not in the calculation of the PWN spectrum. A summary of the parameters and priors is given in Table A1.

## APPENDIX B: POSTERIOR FOR INFERENCE ON A SIMULATED LIGHT CURVE

The posterior for the fit done in Section 3.2 is shown in Figure B1.

This paper has been typeset from a  $\text{TeX}/\text{LaTeX}$  file prepared by the author.

Parameter	Definition	Units	Prior/Value
$M_{\text{ej}}$	Ejecta Mass	$M_{\odot}$	L[0.1, 100]
$L_0$	Initial Magnetar Spin-Down Luminosity	$\text{erg s}^{-1}$	L[ $10^{40}$ , $10^{50}$ ]
$t_{\text{SD}}$	Spin-Down Time	s	L[ $10^2$ , $10^8$ ]
$n$	Magnetar Braking Index		U[1.5, 10]
$\epsilon_B$	Magnetic Field Partition Parameter		L[ $10^{-7}$ , 1]
$\gamma_b$	Electron Injection Lorentz Factor		L[ $10^2$ , $10^7$ ]
$E_{\text{SN}}$	Supernova Explosion Energy	erg	$10^{51}$
$\kappa$	Ejecta Optical Opacity	$\text{cm}^2 \text{ g}^{-1}$	0.1
$\kappa_\gamma$	Ejecta Gamma-Ray Opacity	$\text{cm}^2 \text{ g}^{-1}$	0.01
$q_1$	Low Energy Spectral Index		1.5
$q_2$	High Energy Spectral Index		2.5
$\bar{Z}$	Ejecta Average Atomic Number		8
$Y_e$	Ejecta Electron Fraction		0.5
$Y_{\text{fe}}$	Ejecta Free Electron Fraction		0.0625

**Table A1.** The parameters and default priors implemented for this model. Priors are either uniform (U) or log-uniform (L).

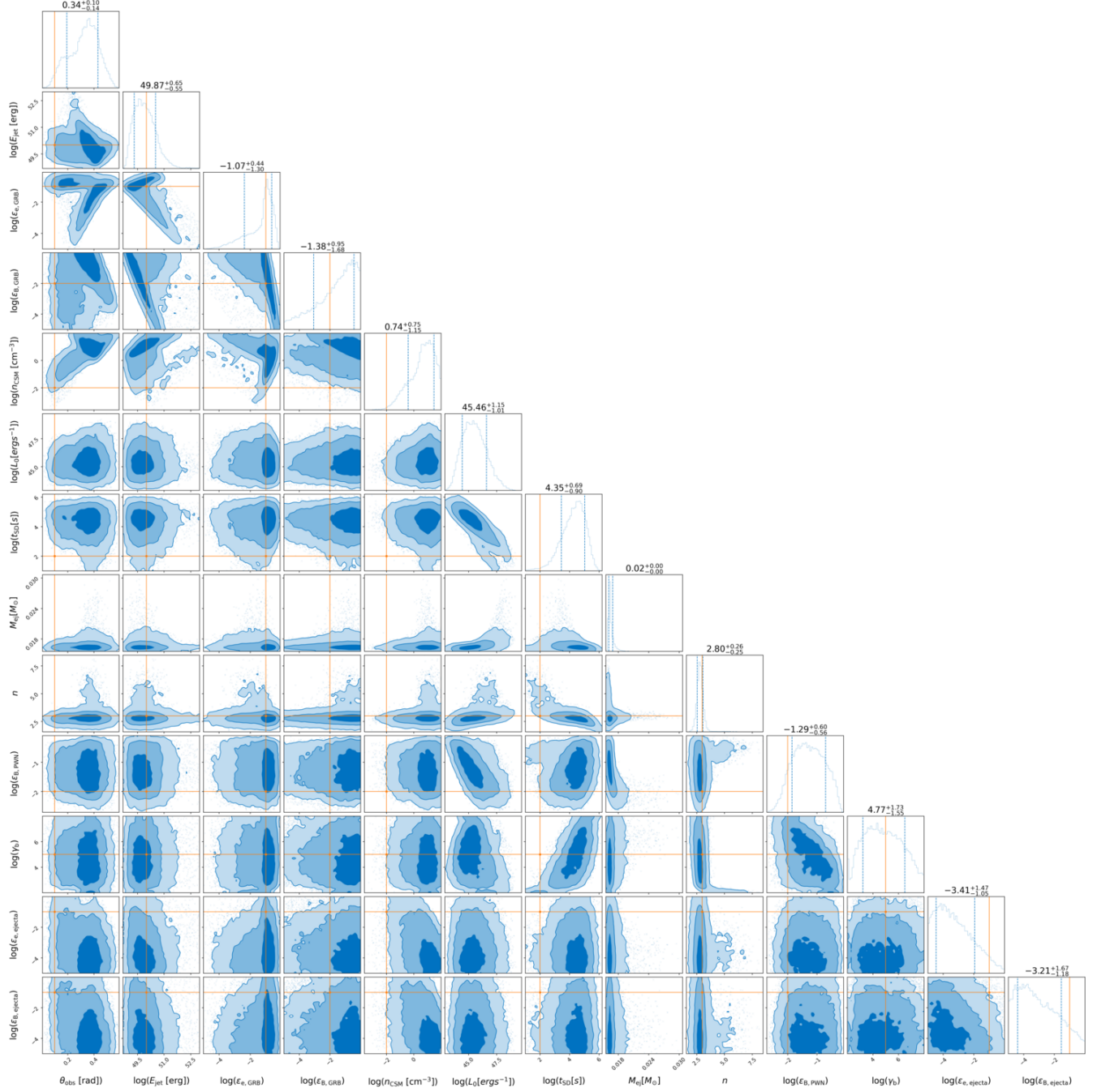


**Figure B1.** The parameter posterior inferred for the simulated kilonova/SGRB. The orange dots and lines indicate the injected parameters.